

Measurements of 3D Channel Impulse Response for Outdoor-to-Indoor Scenario: Capacity Predictions for Different Antenna Arrays

Yawei Yu*, Jianhua Zhang*, Mansoor Shafi[†], Pawel A. Dmochowski[†], Min Zhang[‡] and Jawad Mirza[†]

*Beijing University of Posts and Telecommunications, Beijing, China.

[†]School of Engineering and Computer Science, Victoria University of Wellington, Wellington, New Zealand.

[‡]Spark New Zealand, Wellington, New Zealand.

[‡]Alcatel-Lucent, Swindon, UK.

email: {yyw,jhzhang}@bupt.edu.cn, {pawel.dmochowski,jawad.mirza}@ecs.vuw.ac.nz, mansoor.shafi@spark.co.nz, min.hs.zhang@alcatel-lucent.com

Abstract—We present the results of a 3 dimensional (3D) multiple-input multiple-output (MIMO) channel impulse response (CIR) measurement conducted in China and New Zealand (NZ) for an outdoor-to-indoor (O2I) urban macro environment. Key channel parameters are computed from the measured data using the space-alternating generalized expectation-maximization (SAGE) algorithm, and are used to re-construct the 16×16 3D MIMO CIR according to the guidelines given in the 3GPP 3D MIMO channel model. The CIR is then used to evaluate the channel capacity for four different antenna configurations. These different topologies, along with different antenna spacings, allow us to study the characteristics of the MIMO channel with different spatial correlation structures.

I. INTRODUCTION

Mobile traffic is experiencing an explosive growth due to the wide spread of mobile communication devices and it is predicted that mobile traffic will grow more than 1000 times in the next 10 years [1]. The International Mobile Telecommunications (IMT) vision towards 2020 and beyond requires future 5G systems to deliver a 10 Gbps peak rate. To fulfill such a high spectral efficiency demand, a lot of research activity has been taken place under the umbrella of 5G mobile communication systems. Among these, one important area is 3 dimensional (3D) MIMO, which in addition to the azimuth domain, also takes the elevation domain into consideration, thus providing additional degrees of freedom to meet the high capacity demand [2].

Early research on elevation angle can be traced back to 1979 by T. Aulin, who extended Clark's scattering model to 3D space [3]. World Wireless Initiative New Radio+ (WINNER+) has also reported 3D channel measurements [4]. The 3rd Generation Partnership Project (3GPP) spatial channel model (SCM) has been extended to 3D in [5], along with the investigation of the impact of elevation domain on capacity [6]. Parameters for this standardized 3D channel model have been measured by various contributions [7]–[12]. A comprehensive survey of 3D channel modeling is given in [2]. Despite growing research concerning the 3D space propagation channel model, there are still very few measurements of capacity achievable from various 3D MIMO antenna arrays.

Conventional MIMO antennas utilize only the horizontal

domain. A linear antenna array is typically deployed with vertical polarization or cross-polarization in the horizontal plane at both ends of the communication link, while a fixed downtilting angle is used at base station (BS). Antennas in a rectangular grid or in a cylindrical array, which allocates antenna elements in both azimuth and elevation domain, are not deployed today. Simulation results [13] give a performance comparison between various antenna array configurations, highlighting their effects on system capacity. The authors in [13] only investigate rectangular arrays and do not consider polarization patterns. This paper is a precursor to the capacity that can be achieved with various 3D antenna configurations and different polarizations.

We report the measurement results of 3D CIR in O2I scenario in China and New Zealand (NZ) utilizing 32 antennas at Tx and 56 antennas at Rx. The angular resolution derived from the space-alternating generalized expectation-maximization (SAGE) algorithm [14], through which the effect of antenna patterns on CIR can be eliminated, enables us to re-construct a 16×16 CIR for the 3D channel with various array configurations using the 3GPP 3D MIMO channel model [15]. The main contributions of the paper are summarized below.

- We present measurement results of 3D CIR parameters in an O2I scenario in China and NZ, at carrier frequencies of 3.5 GHz and 2.35 GHz, respectively. Parameters of the 3D CIR are extracted via SAGE, allowing for the reconstruction of a 16×16 3D channel.
- 3D channel capacity is predicted from the measured data. The 16×16 MIMO channel capacity is evaluated for four different antenna topologies: uniform linear antenna array, co-polarized rectangular antenna array, cross-polarized rectangular antenna array and cylindrical antenna array.
- We study the effects of varying inter element antenna spacing and demonstrate that it significantly impacts the channel eigenvalue characteristics.

Results show that large spectral efficiency of 50-70 bps/Hz is achievable even with a 16×16 MIMO channel, depending on the spacing between the antenna elements. Numerical

results also show that the capacities are quite sensitive to the topology of the antenna array, which alters the spatial correlation and results in a different channel rank and eigenvalues structure.

II. MEASUREMENT DESCRIPTION

A. Measurement system

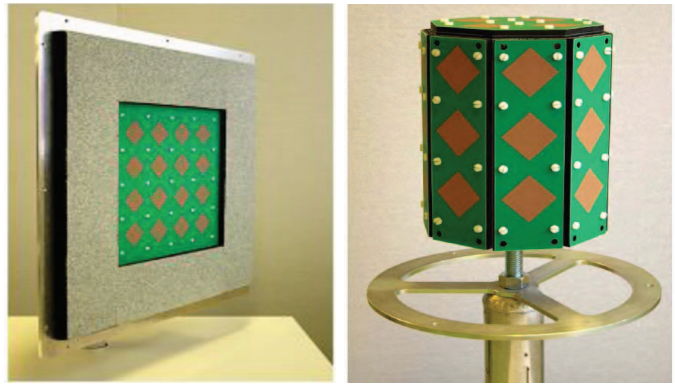
We conducted channel measurements in China and NZ, utilizing the Elektrobit Propsound Sounder described in [16]. To capture the propagation rays in the 3D environment efficiently, fully dimensional antenna arrays were equipped at both sides of the measurement link. The layout of the antenna arrays at Tx and Rx side are illustrated in Fig. 1a and Fig. 1b, respectively. At the Rx, dual-polarized omnidirectional array (ODA) consisting of 56 antenna elements with 8 adjacent sides and a top surface was used, while a dual-polarized uniform planar array (UPA) with 32 antenna elements was utilized as a sector transmit antenna array. All array elements consisted of microstrip patches with 6 dB beamwidth of approximately 110° in both the vertical and horizontal planes. The gain of each antenna element is 6 dBi, with an angle resolution of 2° . This is limited by the sensors' distribution density in the anechoic chamber for antenna calibration, then angle information for paths can be extracted by substituting all possible angle values inside the antenna calibration file iteratively until the reconstructed signal best fits the actual received one [14]. Table I specifies the configuration and angle range of the antenna arrays along with other measurement parameters. The angle ranges capture most of the propagation paths at both ends of the link, where paths with a delay interval larger than the delay resolution can be distinguished. All antennas were calibrated in an anechoic chamber.

TABLE I. ANTENNA CONFIGURATION USED IN MEASUREMENTS

| Parameter | | Value | |
|----------------------------------|-----------|---------------------------------|---------------------------|
| Antenna type | | ODA | UPA |
| Element number | | 56 | 32 |
| Polarized | | $\pm 45^\circ$ | $\pm 45^\circ$ |
| Distribution of antenna elements | | cylinder | planar |
| Angle range | Azimuth | $-180^\circ \sim 180^\circ$ | $-70^\circ \sim 70^\circ$ |
| | Elevation | $-70^\circ \sim 90^\circ$ | $-70^\circ \sim 70^\circ$ |
| Delay resolution | | 20 ns (China), 100 ns (NZ) | |
| Tx power | | 33 dBm (China), 26 dBm (NZ) | |
| PN sequence | | 63 chips (China), 31 chips (NZ) | |

B. Measurement scenario

A key aspect of the 3D CIR measurement in China and NZ was the elevation angle spread in the signal propagation. In the China measurement, the receive antenna array was positioned at 9 different floors of a 60 m high building, while the transmit antenna was fixed at the top of a nearby 11.5 m high building at a distance of 21.5 m. This typical O2I scenario is shown in Fig. 2a, where the layout of the 2nd floor is also illustrated. Walls along the corridor and between the rooms are made of brick, with plasterboard on the surface. The floor is covered with marble, while the doors of the rooms



(a) Tx: 4×4 patches with each patch comprising a pair of cross-polarized antennas. (b) Rx: 8 adjacent sides with 3 patches each, a top surface with 4 patches, each patch contains a pair of cross-polarized antennas.

Fig. 1. Antenna layouts used in the measurements.

are wooden. The Rx was fixed on a trolley with an antenna height of 1.8 m. On each floor, approximately 20 different fixed locations were measured, including ones near the window or along the corridor, with 500 snapshots collected by the sounder for each location. With the exception of the first level, all floors featured a similar layout. Care was taken to ensure identical measurement locations on all floors.

The NZ measurement, shown in Fig. 2b, was performed at a cell site with the Tx antenna installed on the rooftop of a 45 m high building with its boresight pointing to the measurement building, which is approximately 100 m far away. Approximately 80 fixed locations were measured, with 200 snapshots collected for each location.

C. Data post-processing

The field measurements described in Sec. II B provided numerous snapshots of the impulse response of the time-varying radio channel. The collected channel impulse responses were fed to a high-resolution algorithm to estimate the channel parameters for each snapshot. While maximum likelihood estimation (MLE) provides an optimum unbiased estimation from a statistical perspective, it is computationally prohibitive due to the multidimensional searches required. The SAGE algorithm [14] has been proposed as a low-complexity approximation of MLE, and in recent years, has been successfully applied to parameter estimation in channel sounding, eliminating the antenna pattern effects while extracting practical channel propagation information.

III. 3D CHANNEL IMPULSE RESPONSE (CIR)

The parameters extracted from the measurement using the SAGE algorithm were used to populate the 3D CIR based on the model in 3GPP TR 36.873 [15]. Here, the channel matrix is given by

$$\mathbf{H}_{N,M,\tau} = \sum_{l=1}^L \begin{bmatrix} F_{R_x,N,V} \\ F_{R_x,N,H} \end{bmatrix}^T \begin{bmatrix} \alpha_{\tau,l}^{VV} & \alpha_{\tau,l}^{VH} \\ \alpha_{\tau,l}^{HV} & \alpha_{\tau,l}^{HH} \end{bmatrix} \begin{bmatrix} F_{T_x,M,V} \\ F_{T_x,M,H} \end{bmatrix} \quad (1)$$

$$\times \exp(j\hat{r}_{R_x,\tau,l}^T \bar{\mathbf{d}}_N 2\pi\lambda_0^{-1}) \exp(j\hat{r}_{T_x,\tau,l}^T \bar{\mathbf{d}}_M 2\pi\lambda_0^{-1}).$$



Fig. 2. A view of measurement areas in China (a) and NZ (b).

where L is the total number of propagation paths (here, $L = 200$), λ_0 is the wavelength of the carrier frequency¹, $\hat{r}_{Tx,\tau,l}$ and $\hat{r}_{Rx,\tau,l}$ denote the spherical unit vectors at transmitter and receiver elements, respectively, for the l^{th} path with a delay τ . \vec{d}_M and \vec{d}_N are the 3D location vectors for Tx and Rx antennas, respectively, the topology for antennas differs. $F_{Rx,N,V}$ and $F_{Rx,N,H}$ are the receive antenna field patterns for the vertical and horizontal polarizations, respectively, and are given by

$$\begin{bmatrix} F_{Rx,N,V} \\ F_{Rx,N,H} \end{bmatrix} = \begin{bmatrix} \sqrt{A(\vartheta_{\tau,l}, \varphi_{\tau,l})} \cos(\xi) \\ \sqrt{A(\vartheta_{\tau,l}, \varphi_{\tau,l})} \sin(\xi) \end{bmatrix}, \quad (2)$$

where $\varphi_{\tau,l}$ and $\vartheta_{\tau,l}$ are the azimuth angle of arrival (AoA) and elevation AoA, respectively, for the l^{th} path with delay τ . On the Tx side, $F_{Tx,M,V}$ and $F_{Tx,M,H}$ are the transmit antenna field patterns for the vertical and horizontal polarizations, respectively, given by

$$\begin{bmatrix} F_{Tx,M,V} \\ F_{Tx,M,H} \end{bmatrix} = \begin{bmatrix} \sqrt{A(\theta_{\tau,l}, \phi_{\tau,l})} \cos(\xi) \\ \sqrt{A(\theta_{\tau,l}, \phi_{\tau,l})} \sin(\xi) \end{bmatrix}. \quad (3)$$

Here, $\phi_{\tau,l}$ and $\theta_{\tau,l}$ denote the azimuth angle of departure (AoD) and elevation AoD, respectively, for the l^{th} path with delay τ . In (2) and (3), ξ is the antenna slant angle such that for a cross-polarized antenna $\xi = \pm 45^\circ$. The combined antenna pattern (in dB) at Tx is given by [15]

$$A(\theta_{\tau,l}, \phi_{\tau,l}) = -\min[-(A(\theta_{\tau,l}) + A(\phi_{\tau,l})), 30], \quad (4)$$

¹In a slight abuse of notation, we later denote the i^{th} eigenvalue of the channel by λ_i .

where

$$A(\theta_{\tau,l}) = -\min\left[12\left(\frac{\theta_{\tau,l} - 90^\circ}{65^\circ}\right), 30\right], \quad (5)$$

and

$$A(\phi_{\tau,l}) = -\min\left[12\left(\frac{\phi_{\tau,l}}{65^\circ}\right), 30\right]. \quad (6)$$

Similarly, the combined antenna pattern at the Rx is obtained using (4)-(6) with $\vartheta_{\tau,l}$ and $\varphi_{\tau,l}$ replacing $\theta_{\tau,l}$ and $\phi_{\tau,l}$. Finally, the spherical unit vector $\hat{r}_{Tx,\tau,l}$ at the Tx side is given by

$$\hat{r}_{Tx,\tau,l} = \begin{bmatrix} \sin(\theta_{\tau,l}) \cos(\phi_{\tau,l}) \\ \sin(\theta_{\tau,l}) \sin(\phi_{\tau,l}) \\ \cos(\theta_{\tau,l}) \end{bmatrix}. \quad (7)$$

with a similar expression used to obtain the the Rx spherical unit vector using angles $\vartheta_{\tau,l}$ and $\varphi_{\tau,l}$ instead of $\theta_{\tau,l}$ and $\phi_{\tau,l}$.

The following key parameters in (1) were extracted from the measurements and were used to generate each path: 1) complex weights corresponding to different polarization components $[\alpha^{VV}, \alpha^{VH}, \alpha^{HV}, \alpha^{HH}]$, 2) delays τ , 3) azimuth AoD ϕ , 4) azimuth AoA φ , 5) elevation AoD θ , 6) elevation AoA ϑ and 7) Doppler frequency f_d .

IV. 3D CAPACITY CALCULATION

For each measurement location, once the MIMO CIR matrix $\mathbf{H}_{N,M,\tau}$ in (1) is reconstructed using the parameters described in Sec. III, the Discrete Fourier Transform is applied to obtain the channel response matrix $\mathbf{H}_{p,q}$, where p and q denote the location and subcarrier indices, respectively. Then the mean capacity, C , can be calculated by averaging over all fixed spots and subcarriers for four antenna topologies, respectively.

$$C = \frac{1}{PQ} \sum_{p=1}^P \sum_{q=1}^Q \log_2 \det \left(\mathbf{I}_N + \frac{\rho}{\beta M} \mathbf{H}_{p,q} \mathbf{H}_{p,q}^H \right), \quad (8)$$

where ρ is the signal-to-noise ratio (SNR), P and Q are the total number of measurement locations and subcarriers, respectively, and β is a common normalization factor to remove the effects of pathloss, defined by

$$\mathbb{E} \left[\frac{1}{\beta} \|\mathbf{H}_{p,q}\|_F^2 \right] = NM. \quad (9)$$

V. ANTENNA CONFIGURATIONS

The aim of the study is to compare the performance of various antenna configurations in a 16×16 MIMO system. Specifically, we consider four antenna configurations illustrated in Fig. 3: Case A: uniform linear antenna array; Case B: co-polarized rectangular antenna array; Case C: cross-polarized rectangular antenna array and Case D: cylindrical antenna array. We assume that both Tx and Rx consist of 16 antennas in the same configuration.

In Case C, which consists of pairs of cross-polarized antennas, the slant offset angle of cross-polarized antennas is fixed to $\pm 45^\circ$. In Cases A, B and C, the location vectors of Tx and Rx, $\vec{d}_M = \vec{d}_N$, can be trivially computed. In Case D, suppose spacing d is required between the neighboring antennas at a lower circular array with 4 antennas. In this case, the

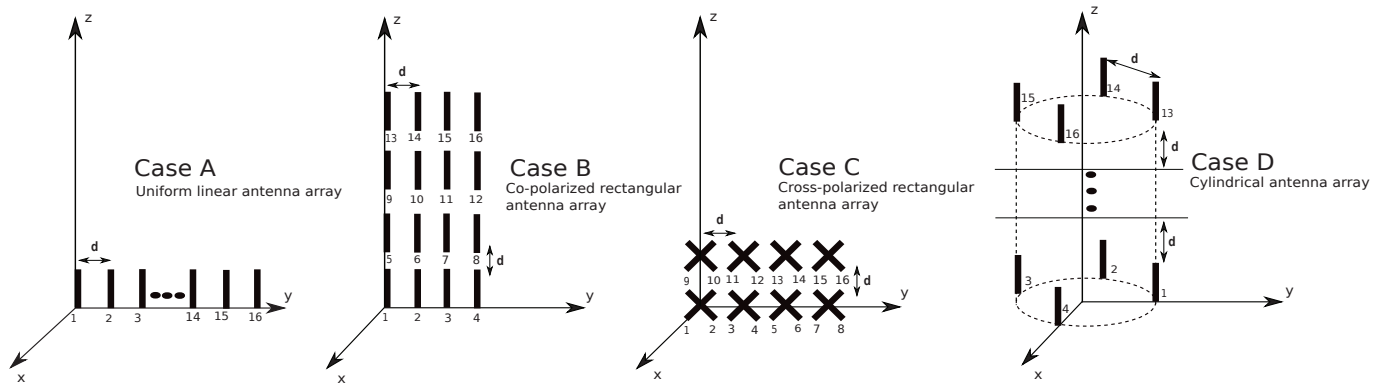


Fig. 3. Antenna configuration cases considered in this paper.

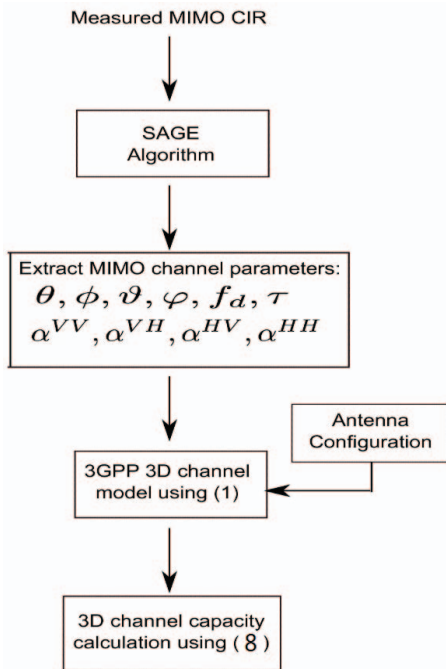


Fig. 4. Flow chart describing the overall process from channel measurements to 3D MIMO channel capacity calculation.

coordinates (x, y, z) are given by $(0, 2d/\pi, 0)$, $(-2d/\pi, 0, 0)$, $(0, -2d/\pi, 0)$ and $(2d/\pi, 0, 0)$, respectively, for antenna 1, 2, 3 and 4. The z coordinate for upper layers in the cylindrical configuration varies with the increment of d .

VI. RESULTS OF MEASUREMENTS

A. Parameters of 3D CIR and MIMO channel matrix

Fig. 4 illustrates the procedure for the 3D MIMO channel capacity calculation based on the measured data. Table II summarizes the distribution of the parameters of the 3D CIR as extracted from the SAGE algorithm and compared with those presented in [15]. Given a particular antenna layout, the position vectors \vec{d}_M and \vec{d}_N are determined. The MIMO channel matrix is then obtained from (1) with (2), (3), (4) and (7) using the parameters extracted.

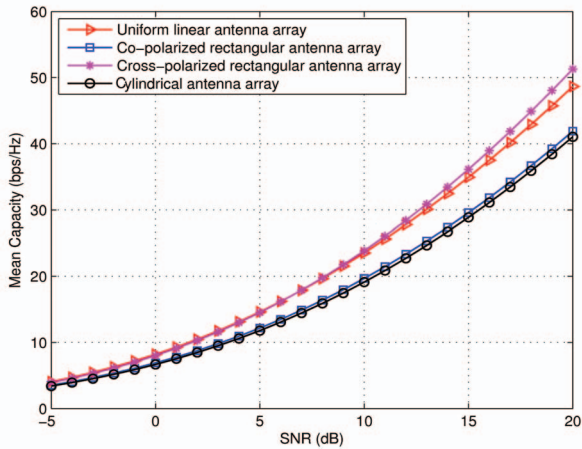
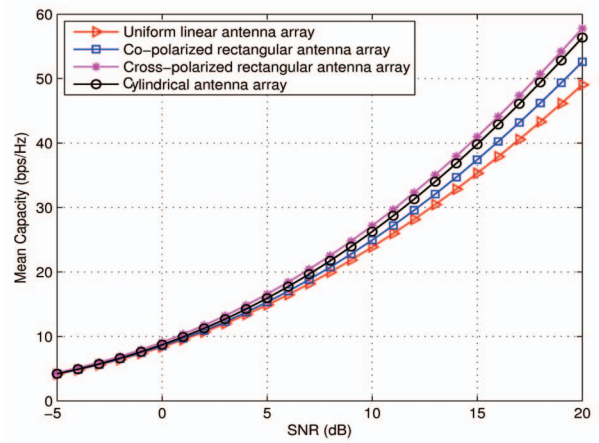
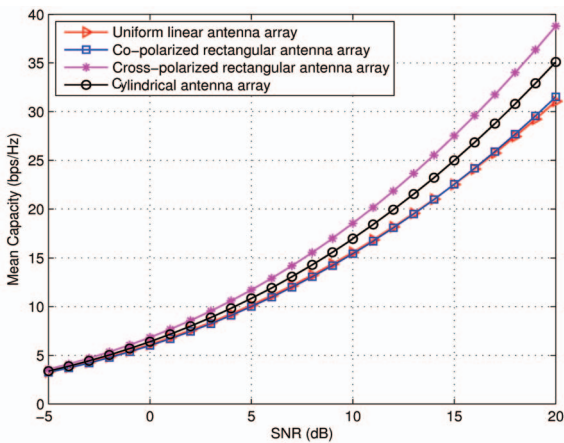
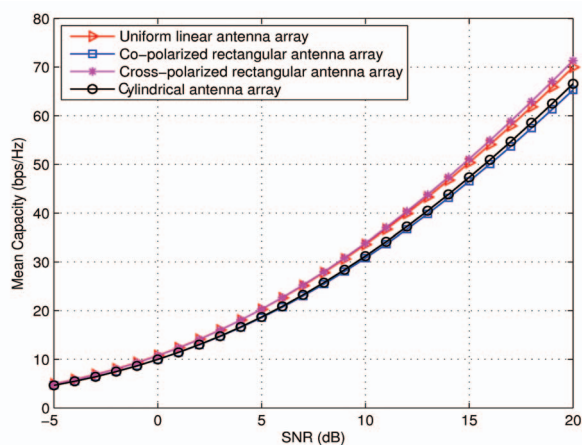
TABLE II. MIMO CHANNEL MODEL PARAMETERS

| Parameters | China | NZ | 3GPP [15] | |
|--|-----------|-------|-----------|-------|
| Delay, τ , spread \log_{10} (s) | μ | -6.62 | -7.96 | -6.62 |
| | σ | 0.32 | 0.25 | 0.32 |
| Azimuth AoD, ϕ , spread \log_{10} (degree) | μ | 1.09 | 1.25 | 1.25 |
| | σ | 0.14 | 0.16 | 0.42 |
| Elevation AoD, θ , spread \log_{10} (degree) | μ | 1.29 | 1.13 | - |
| | σ | 0.10 | 0.28 | - |
| Azimuth AoA, φ , spread \log_{10} (degree) | μ | 1.76 | 1.92 | 1.76 |
| | σ | 0.10 | 0.11 | 0.16 |
| Elevation AoA, ϑ , spread \log_{10} (degree) | μ | 1.37 | 1.56 | 1.01 |
| | σ | 0.14 | 0.10 | 0.43 |
| Cross-polarization Discrimination (XPD) $XPD = 10 \log_{10} \left(\left \frac{\alpha^{VV} + \alpha^{HH}}{\alpha^{HV} + \alpha^{VH}} \right ^2 \right)$ (dB) | μ | 9 | 5.18 | 9 |
| | σ | 11 | 9.05 | 11 |
| Delay distribution | EXP | | | |
| Azimuth AoA and AoD distribution | Gaussian | | | |
| Elevation AoA and AoD distribution | Laplacian | | | |

B. 3D capacity

The 3D CIR computed in Section IV was used to predict the channel capacity for different antenna layouts. With large numbers of antennas to be placed in a limited space, it is prudent to examine the effects of varying the spacing d on the capacity. We show capacity results of two different inter element spacings: $d = \lambda_0$ and $d = 4\lambda_0$, representing closely spaced and moderately spaced antennas.

Figs. 5-6 and Figs. 7-8 present the mean capacity results for all four antenna configurations with $d = \lambda_0$ and $d = 4\lambda_0$, respectively. As expected, both China and NZ measurements for the cross-polarized rectangular array yield the highest ergodic capacity, since the orthogonal configuration of the slant polarized antennas results in low correlation, thus contributing to its capacity superiority. The ergodic capacity performance of the co-polarized rectangular array and cylindrical antenna array are very similar in the China measurements. The negligible difference in the performance between these two topologies was noted in [17], where both topologies exhibit relatively similar spatial correlation. We observe that while the uniform


 Fig. 5. Capacity performance versus SNR for $d = \lambda_0$ (China measurements).

 Fig. 8. Capacity performance versus SNR for $d = 4\lambda_0$ (NZ measurements).

 Fig. 6. Capacity performance versus SNR for $d = \lambda_0$ (NZ measurements).

 Fig. 7. Capacity performance versus SNR for $d = 4\lambda_0$ (China measurements).

linear array is suboptimal in China, it performs the worst in NZ. There, the larger angular spread (AS) in the elevation causes increased scattering in the 3D channel space, and thus the 3D antenna topologies (cross-polarized rectangular and cylindrical antennas) offer larger capacity relative to the

uniform linear array. Referring to Table II, differences in the AS values between China and NZ measurements in both elevation and azimuth are likely responsible for the difference in the capacity performance.

Finally, we consider the effects of antenna correlation on capacity. For the uniform linear array, the number of nearby antennas for each element is two, while this number increases for other configurations. This likely results in a larger correlation, and thus lower capacity. The order of capacity performance curves for the four configuration cases, especially for the uniform linear antenna array, gives important insight into the effects of antenna correlation in practical 3D channels. We note that both China and NZ results are obtained using the same antenna patterns given in (5) and (6), and the 3D CIR parameters are quite similar. The ergodic capacity in China for $d = \lambda_0$ and $d = 4\lambda_0$ shows some gain compared to that in NZ. This is likely due to the fact that the NZ results contain a significant amount of measured line of sight (LoS) propagation paths. It is practically impossible to entirely filter out the LoS data (note that (1) only describes non-line of sight (NLoS) propagation).

C. Eigenvalues

The cumulative distribution functions (CDFs) of the eigenvalue of matrix $(\mathbf{H}_{p,q}\mathbf{H}_{p,q}^H)$ are presented in Fig. 9 and Fig. 10, where due to space limitations we include only the case of $d = 4\lambda_0$. In Fig. 11 we plot the number of contributing eigenvalues, defined as those satisfying $\mathbb{E}[\lambda_i] \geq 1$. We observe that the number of contributing eigenvalues for $d = 4\lambda_0$ is larger than that for $d = \lambda_0$. This is expected, as the rank deficiency of the channel is due to the spatial correlation introduced by the inter element spacing.

VII. CONCLUSION

In this paper we have presented 3D channel capacity and eigenvalue distribution results based on propagation measurements performed in China and NZ. We considered antenna spacing of $d = \lambda_0$ and $d = 4\lambda_0$ in 16×16 MIMO systems. With four different antenna topologies, the parameters of the 3D CIR were extracted from the measured data using the SAGE algorithm. Cross-polarized antennas were found to

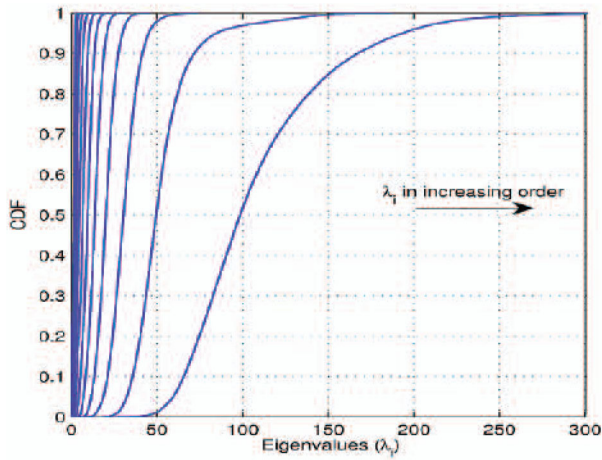


Fig. 9. Contributing eigenvalues CDFs with $d = 4\lambda_0$ for cross-polarized rectangular antenna array in China measurements.

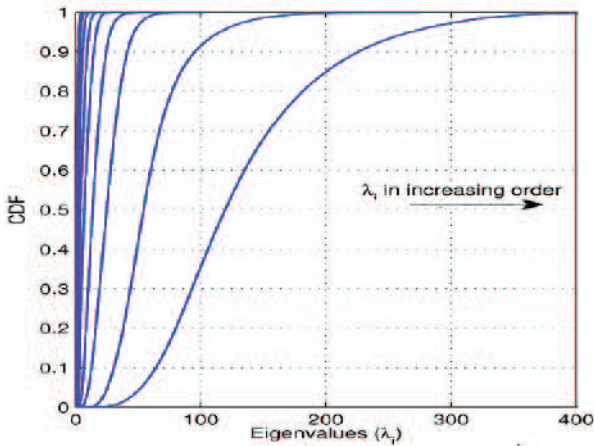


Fig. 10. Contributing eigenvalues CDFs with $d = 4\lambda_0$ for cross-polarized rectangular antenna array in NZ measurements.

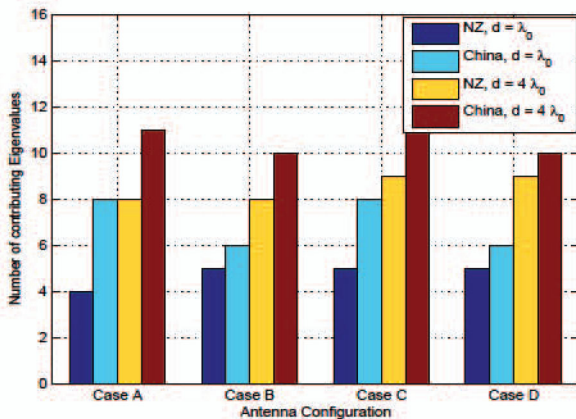


Fig. 11. Number of contributing eigenvalues with $d = \lambda_0$ and $d = 4\lambda_0$ for each antenna configuration case in NZ and China measurements.

perform better than other topologies, making them appropriate choices for 3D MIMO systems. The design of antenna topologies with space constraints and maximum antenna numbers,

proper interval spacing and minimum mutual coupling will be considered in our future work.

VIII. ACKNOWLEDGEMENT

The research is supported by National Natural Science Foundation of China and project name is "Theoretical Modeling and Experiment Research of Propagation Channel" with NO. 61322110; The research is supported by National Key Technology Research and Development Program of the Ministry of Science and Technology of China and project name is "Research and Development for Multi-Dimensional Broadband Time-Varying Channel Emulator" with NO. 2012BAF14B01; The research is supported by National 863 Project of the Ministry of Science and Technology and project name is "High efficiency 5G transmission techniques research" with 2014AA01A705; The research is supported by Ministry of Education Doctoral Fund "3D channel model estimation and beamforming research" with No. 201300051100013.

REFERENCES

- [1] Cisco, "Cisco visual networking index: Global mobile data traffic forecast update, 2013 - 2018," *Cisco White paper*, 2014.
- [2] J. Zhang, C. Pan, F. Pei, G. Liu, and X. Cheng, "Three-dimension fading channel models: a survey of elevation angle research," *IEEE Commun. Mag.*, vol. 52, pp. 218 - 226, June 2014.
- [3] T. Aulin, "A modified model for the fading signal at a mobile radio channel," *IEEE Trans. Veh. Tech.*, vol. 28, no. 3, pp. 182 - 203, 1979.
- [4] J. Meimila, P. Kyosti, L. Henttila, T. Jamsa, E. Sunkkaneen, E. Kumari, and M. Narandzic, "D5.3: WINNER+ Final Channel Models V.1," *Wireless World Initiative New Radio*, 2010.
- [5] M. Shafi, M. Zhang, A. L. Moustakas, P. J. Smith, A. F. Molisch, F. Tufvesson, and S. H. Simon, "Polarized MIMO channels in 3-D: models, measurements and mutual information," *IEEE J. Sel. Areas Commun.*, vol. 24, no. 3, pp. 514 - 527, 2006.
- [6] M. Shafi, M. Zhang, P. J. Smith, A. L. Moustakas, and A. F. Molisch, "The impact of elevation angle on MIMO capacity," in *IEEE Int. Conf. Commun.*, vol. 9, pp. 4155 - 4160, IEEE, 2006.
- [7] 3GPP R1-133525, "Umi channel measurement results on elevation related parameters," CMCC, CATT.
- [8] 3GPP R1-132544, "O2i channel measurements results on elevation related parameters," CMCC, CATT.
- [9] 3GPP R1-132543, "Uma channel measurements results on elevation related parameters," CMCC, CATT.
- [10] 3GPP R1-134221, "Proposals for 3D MIMO channel modelling in uma," Alcatel-Lucent Shanghai Bell, Alcatel-Lucent, China Unicom.
- [11] 3GPP R1-134222, "Proposals for 3D MIMO channel modelling in umi," Alcatel-Lucent Shanghai Bell, Alcatel-Lucent, China Unicom.
- [12] 3GPP R1-134795, "Proposals for 3D MIMO channel modelling in O2i," Alcatel-Lucent Shanghai Bell, Alcatel-Lucent, China Unicom.
- [13] Y.-H. Nam, B. L. Ng, K. Sayana, Y. Li, J. Zhang, Y. Kim, and J. Lee, "Full-dimension MIMO (FD-MIMO) for next generation cellular technology," *IEEE Commun. Mag.*, vol. 51, no. 6, pp. 172 - 179, 2013.
- [14] B. H. Fleury, M. Tschudin, R. Heddergott, D. Dahlhaus, and K. Ingeman Pedersen, "Channel parameter estimation in mobile radio environments using the SAGE algorithm," *IEEE J. Sel. Areas Commun.*, vol. 17, no. 3, pp. 434 - 450, 1999.
- [15] 3GPP TR 36.873 V.2, "Study on 3D channel model for LTE (Release 12)," Technical report, 2014.
- [16] J. Zhang, "Review of wideband MIMO channel measurement and modeling for IMT-advanced systems," *Chinese Science Bulletin*, vol. 57, no. 19, pp. 2387 - 2400, 2012.
- [17] C. T. Neil, M. Shafi, P. J. Smith, and P. A. Douchowaki, "On the impact of antenna topologies for massive MIMO systems," *arXiv preprint arXiv:1503.00789*, 2015.